Supporting Information:

Wurtzite boron arsenide polytypes for polarization-controlled optoelectronic devices: a first-principles study

Cesar E. P. Villegas,*,† Enesio Marinho Jr.,‡ K. Lizárraga,¶ Alexandre C. Dias,§ Rodrigo G. Amorim,⊥ Wanderlã L. Scopel,# and Alexandre R. Rocha@

† *Departamento de Ciencias, Universidad Privada del Norte, Lima 15434, Peru*

‡*Departamento de Física e Química, Faculdade de Engenharia, Universidade Estadual Paulista (UNESP), Av. Brasil 56, 15385-007 Ilha Solteira, São Paulo, Brazil.*

¶*Center for Quantum Nanoscience, Institute for Basic Science (IBS), Seoul 03760, Republic of Korea*

§*Institute of Physics and International Center of Physics, University of Brasília, Brasília, Distrito Federal 70919-970, Brazil*

‖*Computational Materials Laboratory, LCCMat, Institute of Physics, University of Brasília, 70910-900, Brasília, Federal District, Brazil*

⊥*Departamento de Física, ICEx, Universidade Federal Fluminense - UFF, Volta Redonda/RJ, Brazil*

#*Departamento de Física, Universidade Federal do Espírito Santo- UFES , Vitória/ES, Brazil*

@ *Instituto de Física Teórica, Universidade Estadual Paulista (UNESP), R. Dr. Bento Teobaldo Ferraz, 271, São Paulo, 01140-070 São Paulo, Brazil.*

E-mail: cesar.perez@upn.edu.pe

Theory and Methodology

The calculations were carried out within the density functional theory framework, as implemented in the Quantum Espresso package.[1] We employed the Perdew-Burke-Ernzerhof generalized gradient approximation (PBE-GGA) to analyze the ground-state electronic properties, while the local-density approximation (LDA) was used exclusively for the investigation of vibrational properties. We used norm-conserving pseudopotentials and expanded the plane-wave basis set with a kinetic energy cutoff of 90 Ry. The Brillouin zone was sampled using Γ-centered Monkhorst-Pack k-meshes of 12×12×8, 12×12×4, 12×12×3, and 10×10×10 for the 2H, 4H, 6H, and cubic polytypes, respectively. All structures were fully relaxed to their equilibrium positions until residual forces on atoms were smaller than 2 meV/Å. The fully relaxed lattice constants for the 2H, 4H, and 6H-BAs phases were 3.384 Å, 3.391 Å, and 3.394 Å, respectively. These results are consistent with a previous theoretical work that employs the same level of theory.[2]

For the vibrational properties, we employed Brillouin zone sampling grids of 6×6×4, 6×6×3, 6×6×2, and 6×6×6 for the 2H, 4H, 6H, and cubic polytypes, respectively. Based on these grids, density functional perturbation theory (DFPT) is used to compute the vibrational frequencies, normal modes, and dielectric tensor.[3,4] By considering the Placzek approximation, the Raman intensity for a particular normal mode ν with frequency ω associated to the non-resonant Stokes process is obtained as,[5]

$$I^{\nu} \propto |\mathbf{e}_i \cdot A^{\nu} \cdot \mathbf{e}_s|^2 \frac{1}{\omega_\nu}(n_\nu + 1) \tag{1}$$

where $\mathbf{e}_i(\mathbf{e}_s)$ is the incident (scattered) light polarization, n_ν the Bose-Einstein distribution, and A^{ν} is the Raman tensor with matrix elements

$$A^{\nu}_{lm} = \sum_{k\gamma} \frac{\partial^3 \mathcal{E}^{el}}{\partial E_l \partial E_m \partial u_{k\gamma}} \frac{w^{\nu}_{k\gamma}}{\sqrt{M_k}}. \tag{2}$$

Here $\mathcal{E}^{el}$ is the electronic energy of the system in the presence of a uniform electric field $E_{l(m)}$ along $l(m)$, $u_{k\gamma}$ corresponds to the γ-th component of the normal mode on atom k, and M_k is the corresponding atomic mass. We consider light propagating perpendicular to the xz plane, which we denote as a-plane configuration. In this scenario, the incident polarization vector can be written as, $\mathbf{e}_{i,a} = [cos\varphi \;\; 0 \;\; sin\varphi]$, while two possible directions for scattered light—$\mathbf{e}^{\parallel}_{s,a} = [cos\varphi \;\; 0 \;\; sin\varphi]$ and $\mathbf{e}^{\perp}_{s,a} = [-sin\varphi \;\; 0 \;\; cos\varphi]$—are allowed. In Porto notation,[6] these two possibilities are represented as $y(xx)\bar{y} \leftrightarrow y(zz)\bar{y}$ ($\mathbf{e}_i \parallel \mathbf{e}_{s,a}$) and $y(xz)\bar{y} \leftrightarrow y(zx)\bar{y}$ ($\mathbf{e}_i \perp \mathbf{e}_{s,a}$).

To overcome the band gap underestimation of DFT-GGA, quasiparticle (QP) corrections are included within the G_0W_0 approximation. In this framework, the quasiparticle energies are given by,[7]

$$E^{\mathrm{QP}}_{n\mathbf{k}} = \epsilon^{\mathrm{KS}}_{n\mathbf{k}} + Z_{n\mathbf{k}} \left\langle n\mathbf{k}^{\mathrm{KS}} \middle| \Sigma_{n\mathbf{k}}(\epsilon^{\mathrm{KS}}_{n\mathbf{k}}) - V^{\mathrm{xc}}_{n\mathbf{k}} \middle| n\mathbf{k}^{\mathrm{KS}} \right\rangle , \tag{3}$$

where $\left|n\mathbf{k}^{\mathrm{KS}}\right\rangle$, $Z_{n\mathbf{k}}$ and $V^{\mathrm{xc}}_{n\mathbf{k}}$ describe the Kohn-Sham eigenstates, QP renormalization factor, and DFT exchange-correlation potential. The correlation part of the self-energy is defined by $\Sigma_{n\mathbf{k}} = i \int \frac{d\omega'}{2\pi} e^{i\omega' 0^+} \left\langle n\mathbf{k}^{\mathrm{KS}} \middle| G_0(\omega+\omega') W_0(\omega') \middle| n\mathbf{k}^{\mathrm{KS}} \right\rangle$. Here G_0 and W_0 stands for the non-interacting Green's function and the screened Coulomb potential, respectively. The dynamical Coulomb screening matrix is obtained considering the Plasmon-Pole approximation in the Godby-Needs scheme[8] with an energy cutoff of 18 Ry and including 300 bands for both the screening and GW sum-over-states, which is sufficient to provide accurate results owing to the implementation of Bruneval-Gonze terminators.[9] The GW calculations were carry out with Brillouin samples of 6×6×4, 6×6×3, 6×6×3, and 10×10×10 for the 2H, 4H, 6H, and cubic polytypes, respectively. The convergence of the GW parameters is presented in the Supporting Information.

The excitonic effects on the optical absorption spectra are taken into account by solving

the Bethe-Salpeter equation (BSE), which is governed by the excitonic Hamiltonian,[10]

$$H_{cv\mathbf{k},c'v'\mathbf{k}'} = (E^{QP}_{c\mathbf{k}} - E^{QP}_{v\mathbf{k}'})\delta_{cc'}\delta_{vv'}\delta_{\mathbf{k}\mathbf{k}'} + 2v^{v'c'\mathbf{k}'}_{cv\mathbf{k}} - W^{v'c'\mathbf{k}'}_{cv\mathbf{k}}, \tag{4}$$

where the screened (W) and bare (v) Coulomb potentials describe the e-h attraction and repulsive terms, respectively. These two terms are calculated in the same **k**-grid as in the GW calculation and then interpolated on a finer **k**-grid sample of 30×30×20, 30×30×16, 30×30×12, and 30×30×30 for 2H, 4H, 6H and cubic structures, respectively.

Finally, the optical absorption is calculated from the imaginary part of the dielectric function

$$\epsilon_2(\omega) = \frac{8\pi e^2}{VN_k}\sum_S |\mu_S|^2\,\delta(\omega - \Omega^S) \tag{5}$$

where Ω^S is the S-th exciton eigenvalue. $\mu_S = \sum_{vc\mathbf{k}} A^S_{vc\mathbf{k}}\hat{\mathbf{e}}\cdot\langle c\mathbf{k}|\mathbf{r}|v\mathbf{k}\rangle$ represents the excitonic transition dipole matrix elements, being $\hat{\mathbf{e}}$ and $\mathbf{r}$ the polarization vector and position operator, respectively. V and N_k represents the unit cell volume and number of points in the Brillouin zone.

The imaginary part of the dielectric function is computed by including, in the sum over states, the six highest occupied valence bands and the corresponding six lowest unoccupied conduction bands for the 2H and 4H phases, whereas for the 6H phase, the nine highest occupied valence bands and the corresponding nine lowest unoccupied conduction bands are considered. This is sufficient to achieve well-converged optical excitations for both polarizations over the energy range of interest. A Lorentzian function with broadening of 0.12 eV is used to model the delta function in the dielectric response function. The YAMBO code was used to perform the QP and optical calculations.[11] In all our calculations, spin–orbit coupling (SOC) effects are neglected. Although its inclusion leads to a slight renormalization of the electronic states at Γ, the resulting band splittings are smaller than those in c-BAs. Consequently, the impact on the optical response is minimal, owing to the weak oscillator

strengths associated with electronic transitions near the Γ point as demonstrated in Fig. S13.

Convergence analyses for the GW calculations

Figure S1 shows the convergence of the GW parameters of a c-BAs at Γ- and X-point with respect to the number of bands in the self-energy, number of bands in the dielectric constant, screening cutoff, and the **k**-grid sample. The convergence is performed by keeping the parameters one is not interest in converging as high as possible. Thus, during the convergence of the number of bands in the Self-energy and dielectric constant, we kept fixed the screened cutoff to 24 Ry and estimate the error in the quasiparticle (QP) band gap correction at the mentioned symmetry point as the number of bands used is varied. A similar procedure is adopted for converging the screened cutoff. In this case, the numbers of bands in self-energy and dielectric constant is fixed to 1000 while we estimate the error in the QP band gap correction as the screening cutoff is varied. Finally, once the number of bands and the screening cutoff is chosen, we proceed to perform the convergence with respect to the **k**-grid. It should be noticed that our GW calculations present reliable predictions within an accuracy of approximately 0.025 eV. Iin Figure S2 we show the convergence of the GW parameters for wurtzite BAs, similar trends can be observed. However, for this phase the GW results present an accuracy of approximately 0.035 eV.

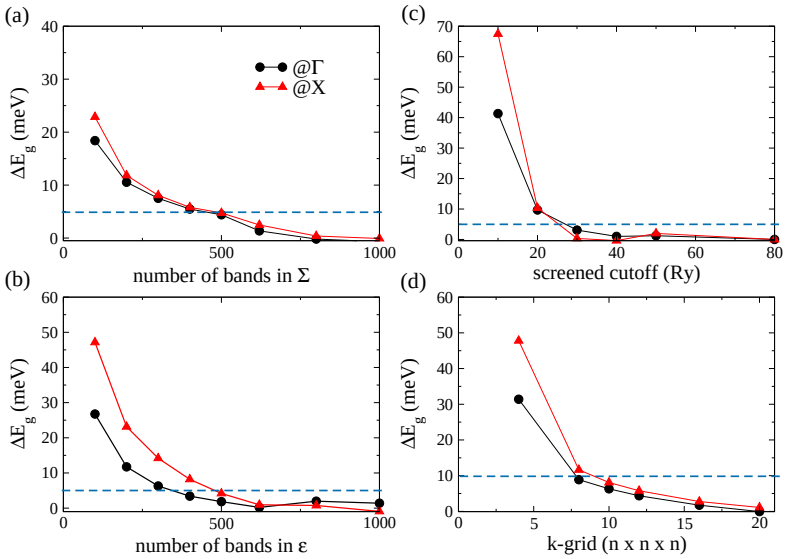

Figure S1: Convergence of *GW* quasiparticle gap for the c-BAs with respect to (a) number of bands in the correlation part of self-energy operator, (b) number of **G**-vectors (energy cutoff) in the dielectric constant, (c) number of bands to construct the response function, and (d) **k**-point grid. The error in quasiparticle (QP) direct band gap is computed at **k**-points Γ and K. The dashed lines represent the chosen values for each GW feature.

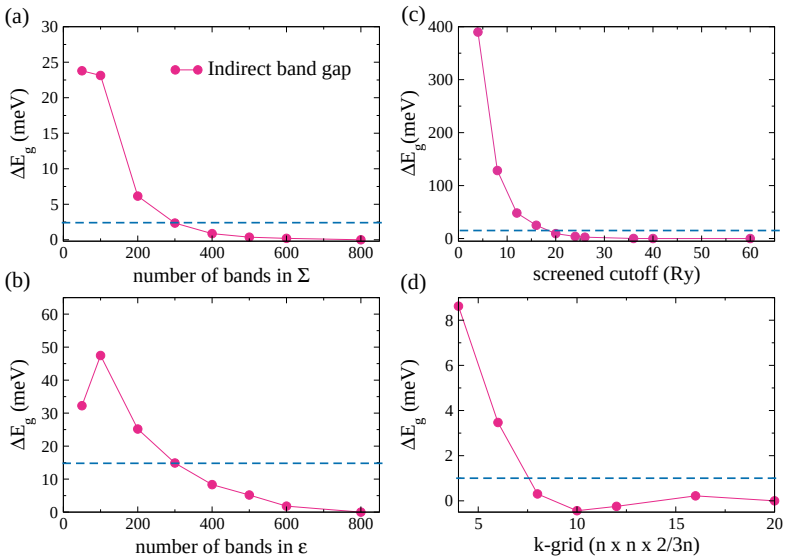

Figure S2: Convergence of *GW* quasiparticle gap for the wurtzite phase of BAs with respect to (a) number of bands in the correlation part of self-energy operator, (b) number of **G**-vectors (energy cutoff) in the dielectric constant, (c) number of bands to construct the response function, and (d) **k**-point grid. The error in quasiparticle (QP) direct band gap is computed at **k**-points Γ and K. The dashed lines represent the chosen values for each GW feature.

Raman intensity polarization

In the study of the Raman polarization effects, it is important to properly define the direction of the incident polarization vector, as well as the rotation angles, as shown in Figure S3. Our study considers light propagating in the a-plane, which we denote as a-plane configuration. In this scenario, the incident polarization vector can be written as, $\mathbf{e}_{i,a} = [cos\varphi \;\; 0 \;\; sin\varphi]$, while two possibilities for scattered light direction, $\mathbf{e}^{\parallel}_{s,a} = [cos\varphi \;\; 0 \;\; sin\varphi]$ and $\mathbf{e}^{\perp}_{s,a} = [-sin\varphi \;\; 0 \;\; cos\varphi]$ are allowed. In addition, considering incident light propagating in the c-plane, which we denote as c-plane configuration, the incident polarization vector can be written as, $\mathbf{e}_{i,c} = [cos\theta \;\; sin\theta \;\; 0]$. Hence, two possibilities for the scattered light direction can be observed: $\mathbf{e}^{\parallel}_{s,c} = [cos\theta \;\; sin\theta \;\; 0]$ and $\mathbf{e}^{\perp}_{s,c} = [-sin\theta \;\; cos\theta \;\; 0]$. The corresponding azimuthal dependence of the Raman active optical modes for the 2H, 4H, and 6H phases are shown in Figures S4, S5, and S6, respectivel

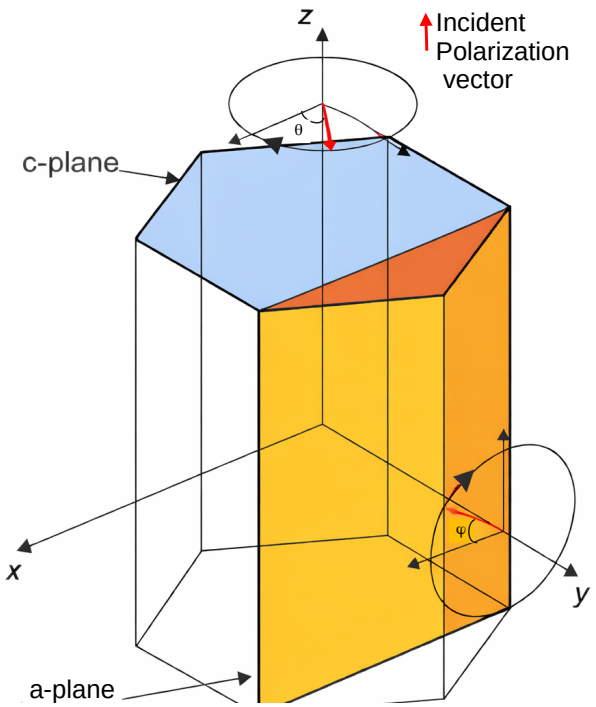

Figure S3: Schematic representation of a wurtzite crystal structure. The orange rectangle represents one of the a-planes which are parallel to the z-axis, while the blue hexagon represents the c-plane which is perpendicular to the z-axis. The red arrows represent the incoming polarization vectors, and the circles around the polarization vectors describe their rotation, being θ and φ the rotation angles with respect to the x-axis

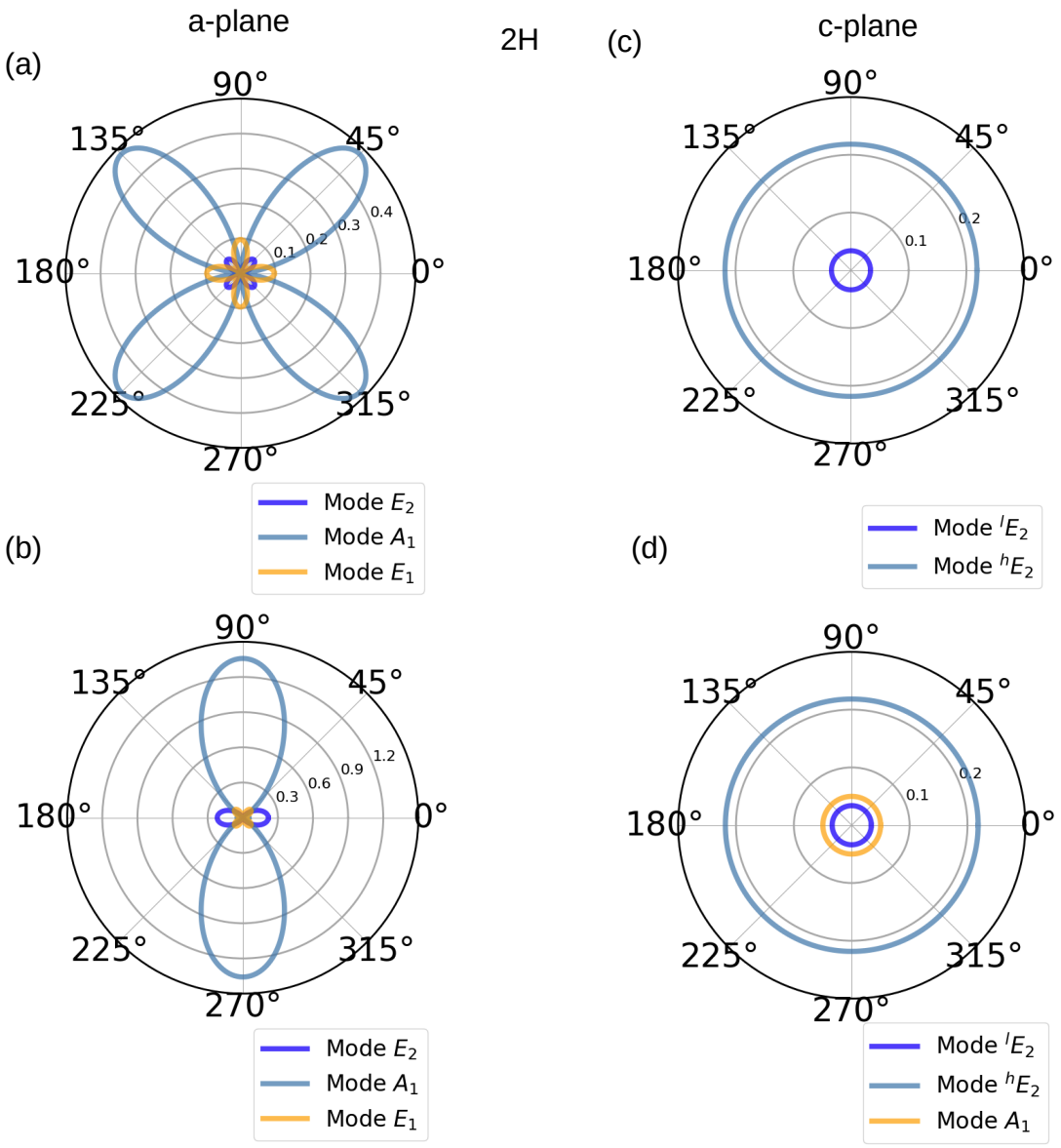

Figure S4: Azimuthal dependence of the Raman active optical modes for the 2H phase of BAs. The angular dependence for the (a) $\mathbf{e}_{i,a} \perp \mathbf{e}_{s,a}$ and (b) $\mathbf{e}_{i,a} \parallel \mathbf{e}_{s,a}$ polarization related to the a-plane configuration are correspondingly shown. Likewise, the angular dependence for the (c) $\mathbf{e}_{i,c} \perp \mathbf{e}_{s,c}$ and (d) $\mathbf{e}_{i,c} \parallel \mathbf{e}_{s,c}$ polarization related to the c-plane configuration are correspondingly shown.

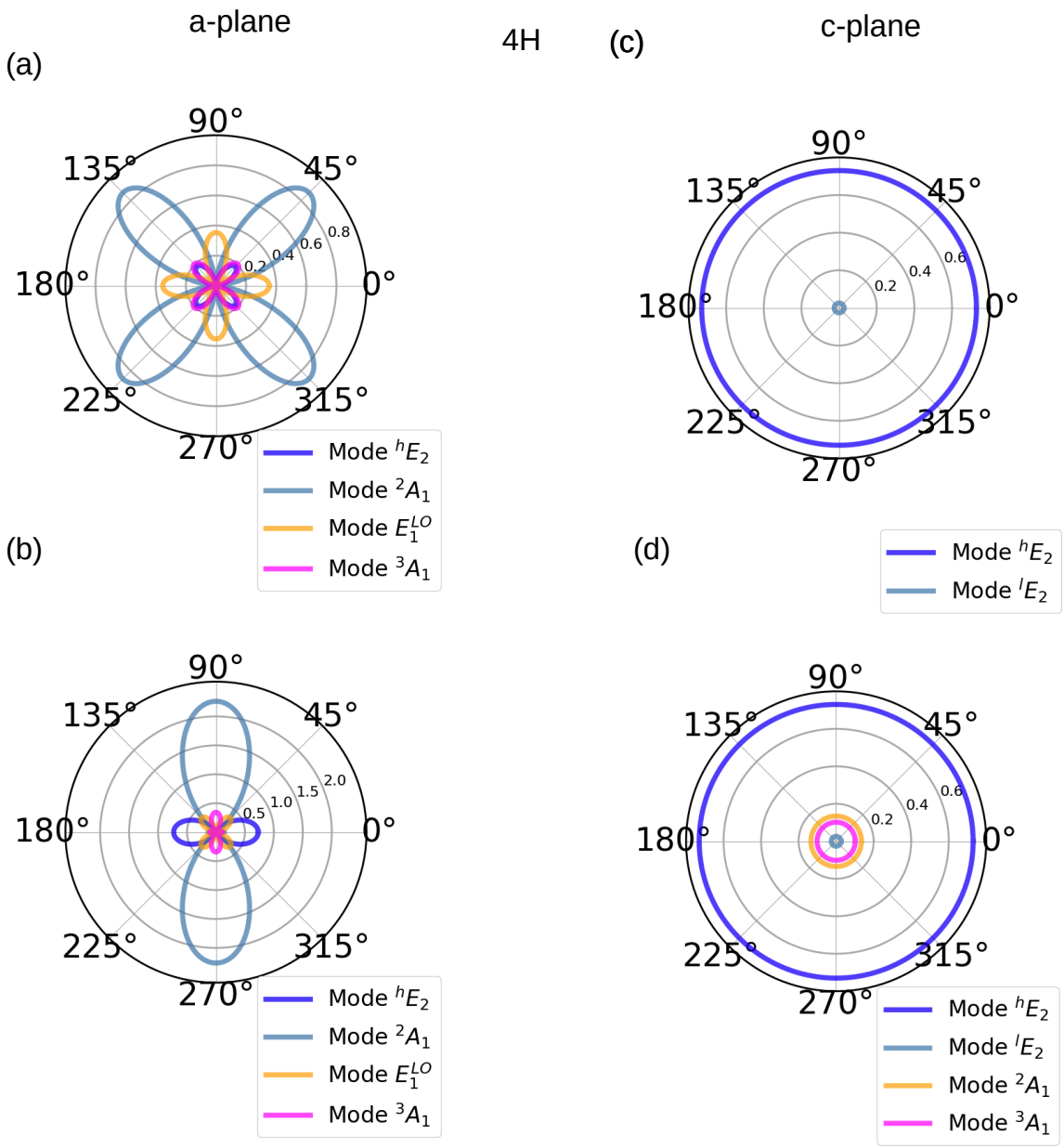

Figure S5: Azimuthal dependence of the Raman active optical modes for the 4H phase of BAs. The angular dependence for the (a) $\mathbf{e}_{i,a} \perp \mathbf{e}_{s,a}$ and (b) $\mathbf{e}_{i,a} \parallel \mathbf{e}_{s,a}$ polarization related to the a-plane configuration are correspondingly shown. Likewise, the angular dependence for the (c) $\mathbf{e}_{i,c} \perp \mathbf{e}_{s,c}$ and (d) $\mathbf{e}_{i,c} \parallel \mathbf{e}_{s,c}$ polarization related to the c-plane configuration are correspondingly shown.

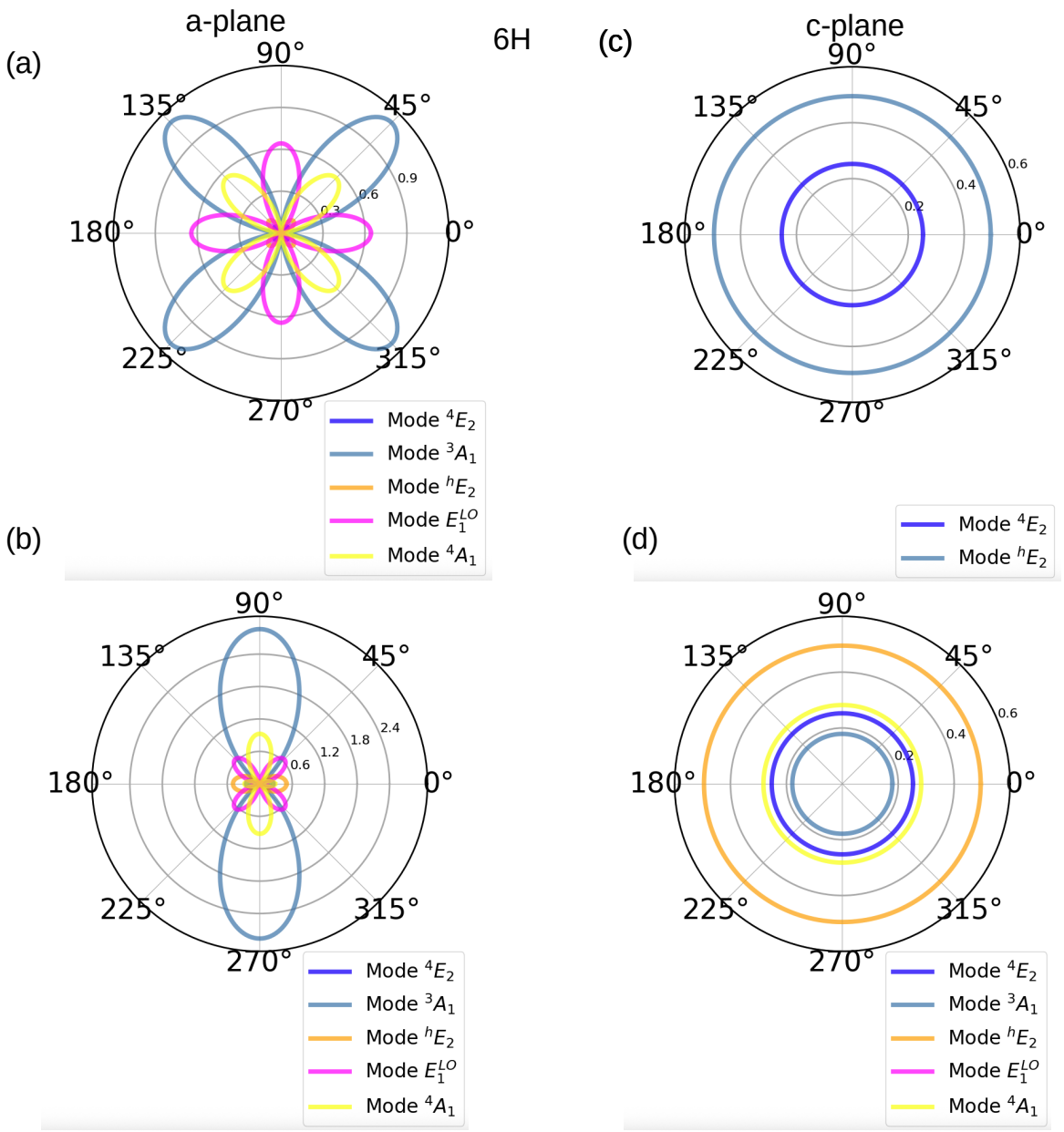

Figure S6: Azimuthal dependence of the Raman active optical modes for the 6H phase of BAs. The angular dependence for the (a) $\mathbf{e}_{i,a} \perp \mathbf{e}_{s,a}$ and (b) $\mathbf{e}_{i,a} \parallel \mathbf{e}_{s,a}$ polarization related to the a-plane configuration are correspondingly shown. Likewise, the angular dependence for the (c) $\mathbf{e}_{i,c} \perp \mathbf{e}_{s,c}$ and (d) $\mathbf{e}_{i,c} \parallel \mathbf{e}_{s,c}$ polarization related to the c-plane configuration are correspondingly shown.

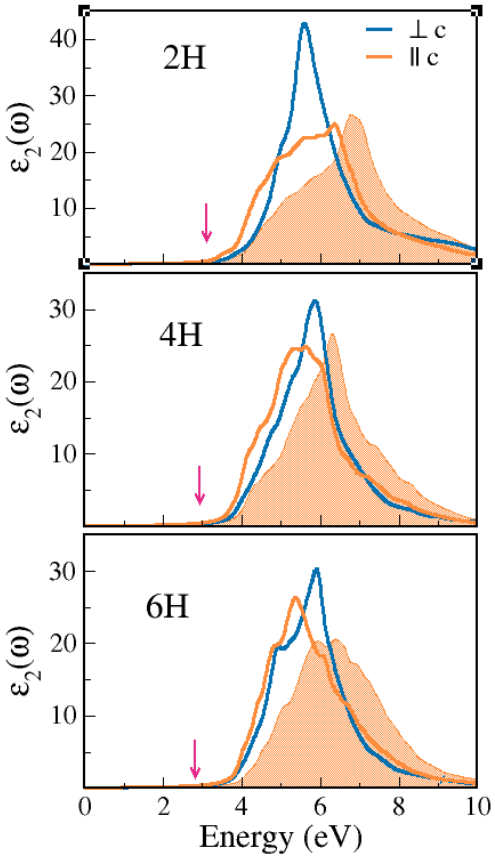

Figure S7: Optical spectra considering ordinary (blue lines) and extraordinary (orange lines light polarizations for different hexagonal BAs polytypes for 2H, 4H, and 6H (from top to bottom). The blue shaded area represents the optical spectra at the independent-particle level that includes the QP corrections from GW calculations only for extraordinary light polarization.

Optical properties

In Figure S7 we present the optical spectra of the hexagonal BAs polytypes (2H, 4H, and 6H) at the GW-BSE (solid lines) and independent particle (I.P) theory level (orange shaded area). Contrary to the figure shown in the main manuscript, here we show the role of the excitonic effects for extraordinary polarization ($\| c$), which can be assessed by comparing the I.P curve with the BSE one. In Figure S8-S10 we show the electronic bands participating in the formation of the most intense peak of the optical absorption, considering $\| c$ and $\perp c$ polarization. Overall, one can see that for the 4H and 6H polytypes the most intense peak arises due to direct electronic transitions along the Γ-M, and H-A, whereas the 2H phase,

transitions are also allowed along the Γ-A path. This results are similar as what occurs in other wurtzite crystals[12–14]

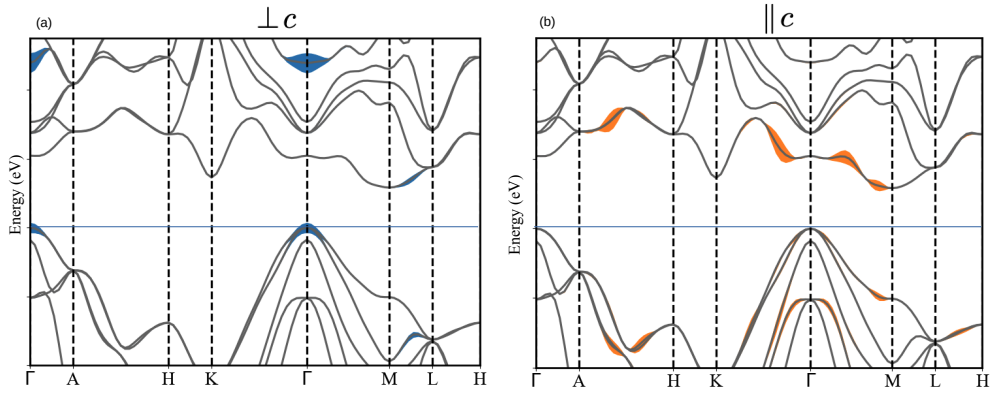

Figure S8: The electronic bands giving rise to the most intense peak in the optical absorption for (a) ⊥ and (b) ∥ polarizations in the 2H phases of BAs. The blue horizontal line represents the Fermi level.

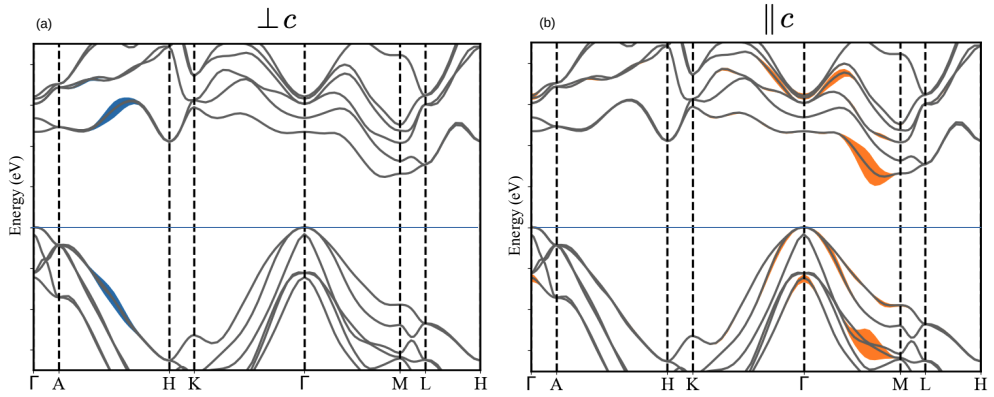

Figure S9: The electronic bands giving rise to the most intense peak in the optical absorption for (a) ⊥ and (b) ∥ polarizations in the 4H phases of BAs. The blue horizontal line represents the Fermi level.

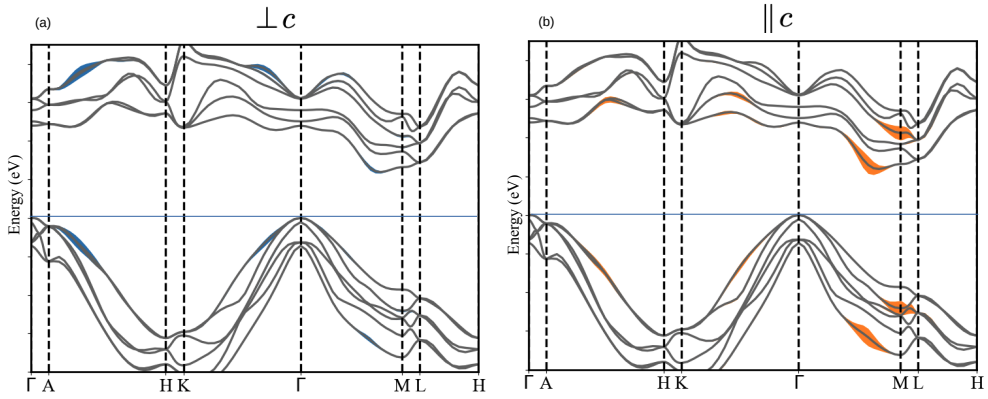

Figure S10: The electronic bands giving rise to the most intense peak in the optical absorption for (a) $\perp$ and (b) $\parallel$ polarizations in the 6H phases of BAs. The blue horizontal line represents the Fermi level.

Spin-orbit coupling effects

For the hexagonal phases considered here, we find that the SOC-induced splitting at the VBM is significantly smaller, decreasing from approximately 0.11 eV in the 2H phase to 0.061 eV in the 6H phase. Additionally, the indirect band gap in these hexagonal polytypes is reduced on average by about 70 meV, which is comparable to the renormalization observed in the cubic phase. Although SOC does affect the electronic structure, we neglect its inclusion because many-body perturbation theory calculations (GW-BSE) with SOC, considering stringent parameters as done in our work, are computationally demanding, particularly for the 4H and 6H phases.

Regarding the impact of SOC on the main features of the optical response, we note that it is not critical for these hexagonal polytypes, unlike in materials such as transition metal dichalcogenides, where A and B excitonic resonances arise from spin–valley coupling selection rules. To support this point, we computed the optical spectra with and without SOC for both c-BAs and the 2H phase (see Fig.S12). The results show that SOC has a minimal effect on the optical response. This behavior can be attributed to the relatively small oscillator strengths of transitions near the Γ point (approximately $\sim$3% of the most intense peak), where SOC-induced band splitting is most pronounced. Since the SOC splitting is even

smaller in the 4H and 6H phases than in the 2H phase, we expect its impact on their optical response to be similarly negligible.

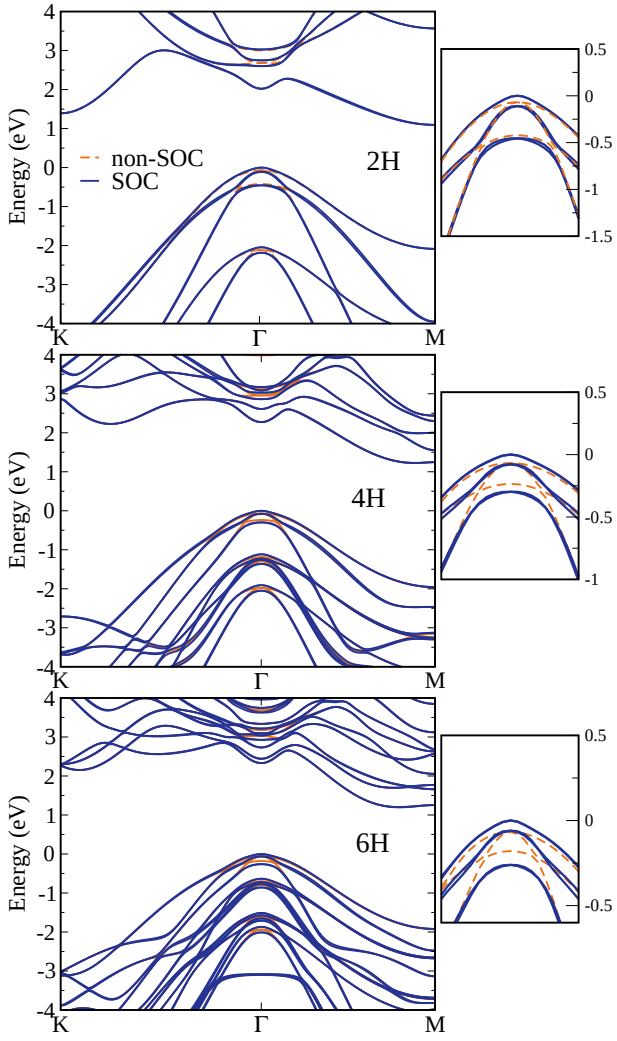

Figure S11: From top to bottom, the figure displays the electronic band structures at the Kohn–Sham level for the $2H$, $4H$, and $6H$ polytypes. The insets provide a magnified view of the region around the Fermi level at the center of the Brillouin zone.

k-resolved projected density of states

The k-pDOS of states on As and B s, px, py , pz orbitals for the 2H, 4H, and 6H polytype are reported in Fig. S13, Fig.S14, and Fig. S15. Based on these information, one can thus

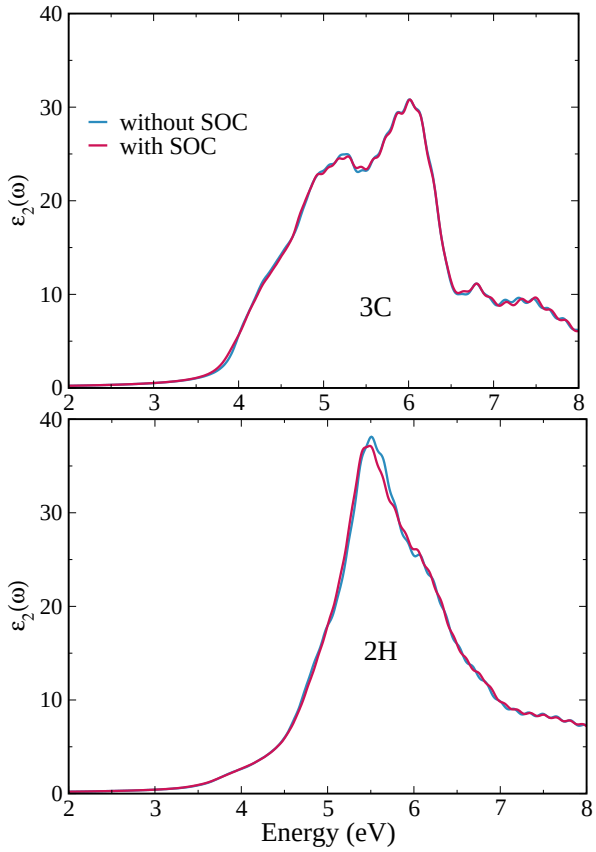

Figure S12: Optical response of the cubic BAs (top panel) and wurtzite BAs (bottom panel) with and without spin-orbit coupling effects. For the 2H phase the light was polarized $\perp$ c.

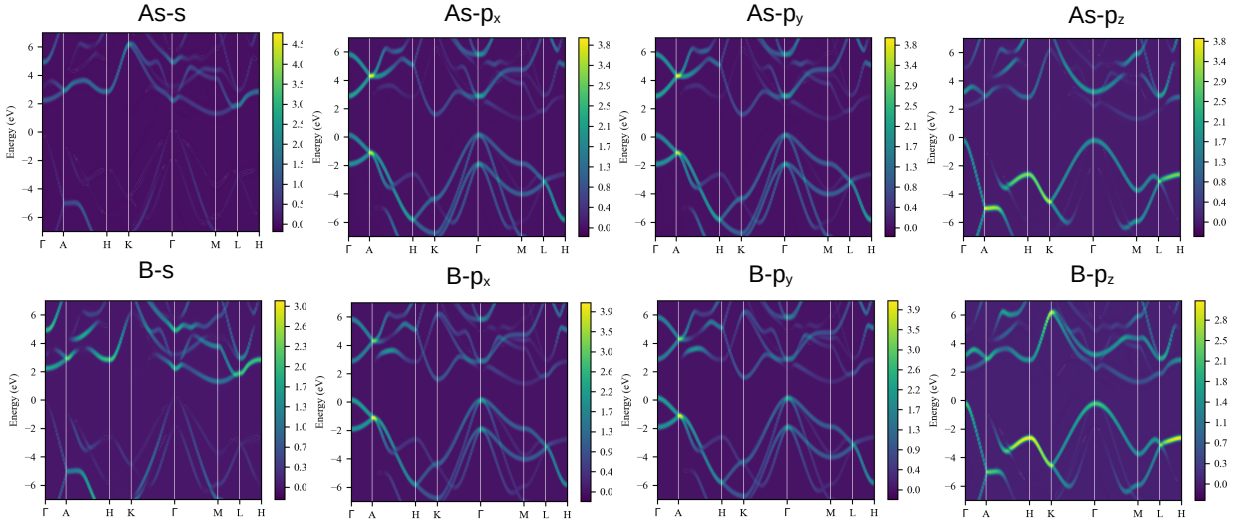

Figure S13: k-resolved pdos for the 2H polytype.

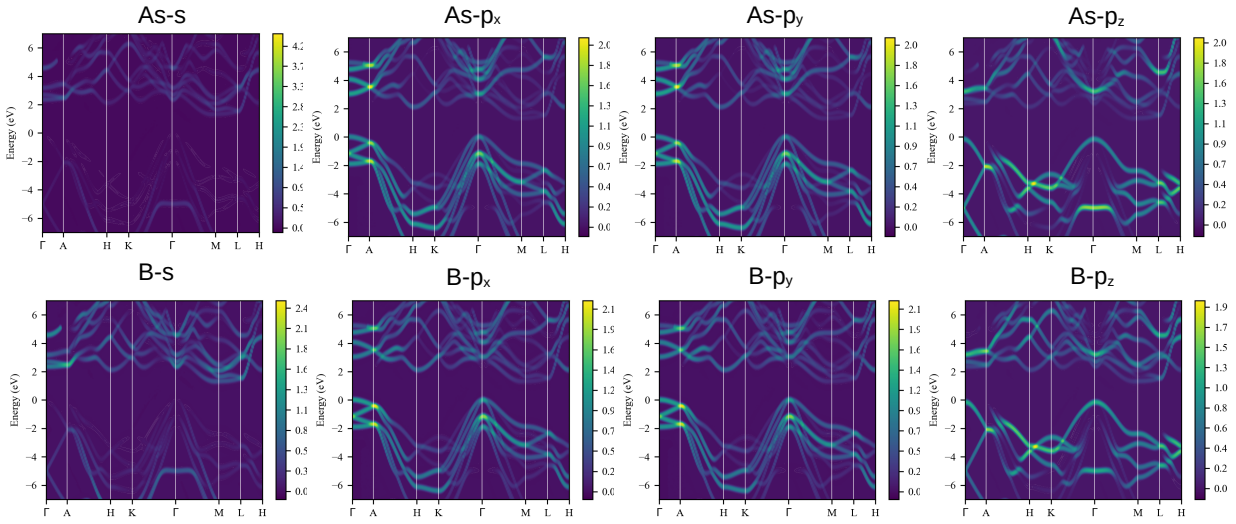

Figure S14: k-resolved pdos for the 4H polytype.

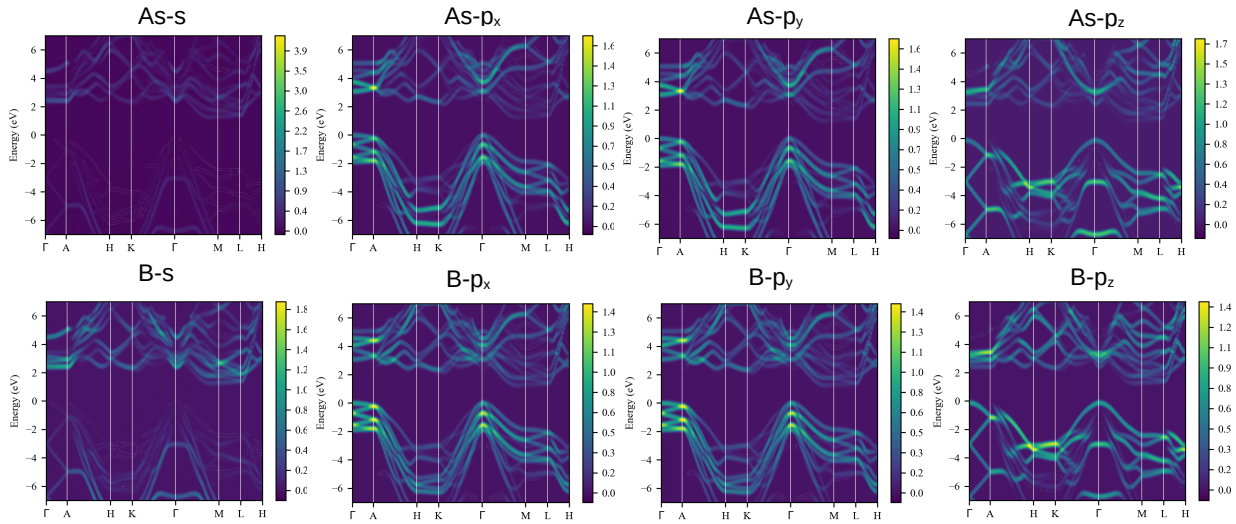

Figure S15: k-resolved pdos for the 6H polytype.

figure out the band composition of the excitonic transitions.

References

(1) Giannozzi, P.; Baroni, S.; Bonini, N.; Calandra, M.; Car, R.; Cavazzoni, C.; Ceresoli, D.; Chiarotti, G. L.; Cococcioni, M.; Dabo, I.; et al. Quantum Espresso: a modular and open-source software project for quantum simulations of materials. *J. Phys.: Condens. Matter* **2009**, *21*, 395502.

(2) Wang, L.; Tian, F.; Liang, X.; Fu, Y.; Mu, X.; Sun, J.; Zhou, X.-F.; Luo, K.; Zhang, Y.; Zhao, Z.; others High-pressure phases of boron arsenide with potential high thermal conductivity. *Phys. Rev. B* **2019**, *99*, 174104.

(3) Giannozzi, P.; De Gironcoli, S.; Pavone, P.; Baroni, S. Ab initio calculation of phonon dispersions in semiconductors. *Phys. Rev. B* **1991**, *43*, 7231.

(4) Baroni, S.; De Gironcoli, S.; Dal Corso, A.; Giannozzi, P. Phonons and related crystal properties from density-functional perturbation theory. *Rev. Mod. Phys.* **2001**, *73*, 515.

(5) Lazzeri, M.; Mauri, F. First-Principles Calculation of Vibrational Raman Spectra in Large Systems: Signature of Small Rings in Crystalline SiO_2. *Phys. Rev. Lett.* **2003**, *90*, 036401.

(6) Damen, T. C.; Porto, S. P. S.; Tell, B. J. P. R. Raman effect in zinc oxide. *Phys. Rev.* **1966**, *142*, 570.

(7) Onida, G.; Reining, L.; Rubio, A. Electronic excitations: density-functional versus many-body Green's-function approaches. *Rev. Mod. Phys.* **2002**, *74*, 601.

(8) Godby, R. W.; Needs, R. J. Metal-insulator transition in Kohn-Sham theory and quasi-particle theory. *Phys. Rev. Lett.* **1989**, *62*, 1169.

(9) Bruneval, F.; Gonze, X. Accurate GW self-energies in a plane-wave basis using only a few empty states: Towards large systems. *Phys. Rev. B* **2008**, *78*, 085125.

(10) Rohlfing, M.; Louie, S. G. Electron-hole excitations and optical spectra from first principles. *Phys. Rev. B* **2000**, *62*, 4927–4944.

(11) Sangalli, D.; Ferretti, A.; Miranda, H.; Attaccalite, C.; Marri, I.; Cannuccia, E.; Melo, P.; Marsili, M.; Paleari, F.; Marrazzo, A.; others Many-body perturbation theory calculations using the yambo code. *J. Phys. Condens. Matter.* **2019**, *31*, 325902.

(12) Rödl, C.; Sander, T.; Bechstedt, F.; Vidal, J.; Olsson, P.; Laribi, S.; Guillemoles, J.-F. Wurtzite silicon as a potential absorber in photovoltaics: Tailoring the optical absorption by applying strain. *Physical Review B* **2015**, *92*, 045207.

(13) Lambrecht, W.; Segall, B.; Rife, J.; Hunter, W.; Wickenden, D. UV reflectivity of GaN: Theory and experiment. *Physical Review B* **1995**, *51*, 13516.

(14) Cardona, M.; Harbeke, G. Optical properties and band structure of wurtzite-type crystals and rutile. *Physical Review* **1965**, *137*, A1467.